Research Square

Preprints are preliminary reports that have not undergone peer review.
They should not be considered conclusive, used to inform clinical practice,
or referenced by the media as validated information.

Endothelial Sialyl Lewis X-Modified Integrin α3 Drives Fatty Acid Metabolic Reprogramming to Shape Th17 Plasticity in Bladder Cancer

Feng Guan

guanfeng@nwu.edu.cn

Northwest University https://orcid.org/0000-0002-6251-2592

Hui Feng

College of Life Sciences, Northwest University

Huina Zhang

Northwest University

Article

Keywords: sialyl Lewis X, integrin α3, tumor endothelial cells, Th17 plasticity, fatty acid oxidation

Posted Date: April 11th, 2026

DOI: https://doi.org/10.21203/rs.3.rs-9075517/v1

License: This work is licensed under a Creative Commons Attribution 4.0 International License.
Read Full License

Additional Declarations: (Not answered)

Abstract

Tumor endothelial cells (TECs) are active regulators of the tumor immune microenvironment, and their surfaces are enriched with diverse glycans, yet the mechanisms linking endothelial glycosylation to immune modulation remain unclear. Here, we show that sialyl Lewis X (sLeX) glycosylation of integrin α3 (ITGA3) in TECs promotes endothelial-to-mesenchymal transition (Endo-MT) by stabilizing Slug and repressing CDH5 transcription via the EGFR-AKT-GSK3β axis. This process is accompanied by downregulation of aldehyde dehydrogenase 3 family, member A2 (FALDH), with impaired fatty acid oxidation and decreased mitochondrial ROS. Reduced ROS levels suppress the secretion of pro-inflammatory cytokines IL1β and IL6 while enhancing TGFβ production, skewing $CD4^+$ T cell differentiation toward Treg-like Th17 while reducing Th1-like Th17 cells. Functionally, sLeX-modified ITGA3 fosters an immunosuppressive and pro-tumorigenic microenvironment. These findings reveal a novel link between endothelial glycosylation, metabolic reprogramming, and immune regulation, highlighting sLeX-modified ITGA3 as a potential mediator of tumor immune evasion.

Introduction

Cancer remains a leading cause of morbidity and mortality worldwide, with many tumor types characterized by profoundly immunosuppressive microenvironments that limit the efficacy of immunotherapies [1-3]. Among the diverse cellular components of the tumor microenvironment (TME), the vasculature has emerged as a critical regulator of cancer immunity.

TECs are key components of the TME, playing essential roles beyond angiogenesis and vascular remodeling. Once regarded merely as structural elements of the vascular barrier, TECs are now recognized as dynamic regulators in immune surveillance and tolerance [4]. Tumor vasculature often exhibits structural and functional abnormalities, such as excessive permeability and disrupted junctions, which reshape the immune landscape through altered antigen presentation [5, 6] and ligand-receptor signaling [7], ultimately promoting immune cell exclusion and tolerance [8, 9]. Increasing evidence indicates that TECs actively modulate anti-tumor immunity by regulating immune cell recruitment and differentiation, including macrophage function and T-cell responses [10-12]. These insights highlight the vascular niche as a critical determinant of immune evasion and therapeutic resistance.

Endo-MT, in which endothelial cells (ECs) lose junctional integrity and acquire mesenchymal features, has been implicated in extracellular matrix remodeling and immune evasion [13, 14]. However, the molecular mechanisms driving Endo-MT in TECs and its consequences on anti-tumor immunity remain incompletely understood.

The vascular luminal surface is covered by a glycocalyx layer, composed of proteoglycans, glycoproteins, and glycolipids, which orchestrates diverse processes including adhesion, signaling, and molecular transport [15]. Glycosylation modifications in ECs have been linked to developmental and pathological transitions—for example, N-glycan biosynthesis in ECs regulates endothelial-to-hematopoietic transition [16], and O-GlcNAcylation can mediate endothelial metabolic memory in cardiovascular disease [17]. Our

previous study showed that small extracellular vesicles (sEVs) derived from BLCA, enriched in sLeX, are internalized by ECs in an E-selectin-dependent manner. The sLeX modification stabilizes ITGA3, thereby increasing vascular permeability and facilitating metastatic dissemination [18]. Recent work further demonstrated that tumor-cell derived sialylated integrin α3β1 engages Siglec-10 on tumor-associated macrophages to suppress phagocytosis and mediate immune evasion in pancreatic cancer [19]. However, whether sLeX-glycosylated ITGA3 in TECs also governs endothelial phenotypic plasticity and reshapes the immune microenvironment remains unknown.

Here, we show that sLeX-modified ITGA3 promotes Endo-MT and reprograms fatty acid (FA) metabolism in TECs, which in turn impairs their ability to support Th17 differentiation. Th17 cells, a plastic $CD4^+$ T cell subset, exert dual roles in cancer [20, 21]: they can acquire a Th1-like phenotype that produce IFNγ and display enhanced anti-tumor activity [22, 23], or convert into regulatory T cells (Tregs) with potent immunosuppressive functions [24]. By attenuating Th1-like Th17 differentiation while favoring Treg-like Th17 responses, sLeX-modified ITGA3 establishes a glycosylation-metabolism-immunity axis that facilitates tumor immune evasion. These findings expand our understanding of TECs-immune crosstalk in BLCA and suggest novel vascular-targeted strategies for immunomodulation.

Material and methods

Cell lines and cell culture

HUVECs (RRID:CVCL_2959), embryonic kidney 293T cells (HEK-293T, RRID:CVCL_0063), human T lymphoblast-like cell line Jurkat (RRID:CVCL_0065), human THP-1 monocytic cells (RRID:CVCL_0006), and murine bladder carcinoma cell line MB49 (RRID:CVCL_7076) were from the Cell Bank of the Chinese Academy of Sciences (Shanghai). Jurkat were cultured in RPMI 1640. THP-1 were cultured with RPMI-1640 supplemented 0.05 mM β-mercaptoethanol (M3148; Sigma-Aldrich St. Louis, MO, USA). HUVECs, MB49, HEK-293T were cultured in high glucose-DMEM. Cells were cultured in above medium supplemented with 10% fetal bovine serum (Biological Industries; Beit Haemek, Israel) and 1% penicillin/streptomycin (Basalmedia Technologies Co., Ltd., Shanghai, China) at 37°C in a 5% CO_2 atmosphere.

Antibodies and reagents

Antibodies used in this study: sLeX (#563527, RRID:AB_2738259) was from BD Biosciences (Franklin Lakes, NJ, USA). β-tubulin (#2128, RRID:AB_823664), CPT1A (#12252, RRID:AB_2797857), EGF Receptor (#4267, RRID:AB_2246311), phospho-EGF Receptor (Tyr1068) (#3777, RRID:AB_2096270), Akt (#4685, RRID:AB_2225340), phospho-Akt (Ser473) (#4060, RRID:AB_2315049), GSK-3β (#9315, RRID:AB_490890) and Slug (#9585, RRID:AB_2239535) were from Cell Signaling Technology (Beverly, MA, USA). AMPKα1 (A1229, RRID:AB_2759147), phospho-AMPKα1-S485 (AP0871, RRID:AB_2771450), PPARα (A6697, RRID:AB_2767281), IL1β (A22257), IL6 (A0286, RRID:AB_3698196), TGFβ (A21245, RRID:AB_3105906), STAT3 (A11216, RRID:AB_2758462), phospho-STAT3-Y705 (AP0705, RRID:AB_2863810) and RORγt (A10240, RRID:AB_2757766) were from ABclonal (Wuhan, China). FALDH

(sc-373921, RRID:AB_10918012), ITGA3 (sc-374242, RRID:AB_10985868), ITGB1 (sc-9970, RRID:AB_627004), Ubiquitin (sc-8017, RRID:AB_628423), IL17 (sc-374218, RRID:AB_10988239), IFNγ (sc-8423, RRID:AB_627778), FOXP3 (sc-53876, RRID:AB_783444), Twist (sc-81417, RRID:AB_1130910), CD31 (sc-53411, RRID:AB_629040), VE-Cadherin (sc-9989, RRID:AB_2077957), vWF (sc-53466, RRID:AB_630439), Fibronectin (sc-271098, RRID:AB_10608215), Vimentin (sc-6260, RRID:AB_628437) and p-GSK3 α/β (sc-81496, RRID:AB_1125866) were from Santa Cruz Biotechnology (Santa Cruz, CA, USA). FUT7 (#18197-1-AP, RRID:AB_2878516) was from ProteinTech (Rosemont, IL, USA). α-SMA (A2547, RRID:AB_476701) was from Sigma-Aldrich. Snail1 (M021414) was from Abmart (Shanghai, China). HA tag rabbit polyclonal antibody (AF0039, RRID:AB_2939056) was from Beyotime (Shanghai, China).

Plasmids and transfection

The human promoter sequence of VE-cadherin (*CDH5*; Gene ID: 1003) was amplified by PCR from HUVECs genomic DNA extracted using a Genomic DNA Kit (TIANGEN, Beijing, China; DP304). The full-length promoter and its mutant variant were subcloned into the pGL3-Basic (RRID:Addgene_11994) vector (*Xho* I/*Hin*d III). Human cDNA sequences of Slug (*Snail2*; Gene ID: 6591) and FALDH (*ALDH3A2*, Gene ID: 224) were amplified by PCR, and subcloned into the pLVX-AcGFP1-N1 (RRID:Addgene_54705) vector (*Xho* I/*Bam*H I) and pLVX-IRES-Neo vector (*Eco*R I/*Not* I) with an C-terminal Flag tag, respectively. Mouse *FUT7* cDNA was subcloned into the pLV11ltr-Puro-mCherry-CMV (RRID:Addgene_123221) vector (*Xho* I/*Bam*H I). All constructs were verified by Sanger sequencing. Plasmid transfections were performed in serum-free medium using PEI MAX (Polysciences, USA) according to the manufacturer's instructions.

CRISPR/sgRNA transduction

Single guide RNA (sgRNA) sequence targeting human *FALDH* and mouse *FUT7* were cloned into lentiCRISPR v2-NEO (RRID:Addgene_104992) vector. The DNA oligonucleotides used for sgRNA cloning are listed in **Table S1**. HEK-293T cells were transfected with mixed lentiCRISPR and packing vectors. Target cells were transduced with the lentivirus expressing *FALDH* or *FUT7* sgRNA in the presence of PEI MAX for 24 h.

Chromatin immunoprecipitation

Chromatin immunoprecipitation (ChIP) assays were conducted using a ChIP Assay kit (P2078, Beyotime) as described previously [12]. Briefly, cells were cross-linked with 1% formaldehyde for 10 min at room temperature (RT) and incubated with glycine for 5 min. After washing with precooled PBS, cells were lysed into SDS lysis buffer (containing 1mM PMSF) on ice for 10 min and centrifuged at 14, 000 *g* for 5 min at 4℃. Nucleic lysates were sonicated (10 cycles, 8 s each with 30 s interval) on ice. Sheared chromatin was incubated with anti-Slug (20 μg; sc-166476 X, Santa Cruz) or control IgG (20 μg; #5415, Cell Signaling Technology, RRID:AB_10829607) overnight at 4°C, followed by bound to protein A+G Agarose/Salmon Sperm DNA for 4 h at 4°C and washed sequentially. DNA was eluted (1% SDS and 0.1M

$NaHCO_3$), reverse cross-linking at 65°C for 4 h (50 mM NaCl), and then treated with TE buffer (40 mM Tris-HCl, pH 6.5; 10 mM EDTA and 40 μg/mL proteinase K) at 45°C for 1 h. DNA was purified by Tris-equilibrated phenol-chloroform extraction, ethanol precipitation (3 M sodium acetate, glycogen carrier), and centrifugation at 14, 000 *g* for 10 min at 4 °C. The recovered DNA was analyzed by quantitative real-time PCR (qRT-PCR) using primers listed in **Table S1**.

Luciferase reporter assay

The assay was performed as described previously [25]. Cells (1×10^5/well) were seeded in 24-well plates and co-transfected with *CDH5* promoter-pGL3-basic (Firefly luciferase), pRL-TK (RRID:Addgene_11313, *Renilla* luciferase), and pLVX-AcGFP1-N1-Slug plasmids at a ratio of 10:1:10. After 4-6 h of transfection, the medium was replaced with DMEM containing 10% FBS, and cells further were cultured for 48 h. Luciferase activity was measured using the Dual Luciferase Reporter Gene Assay Kit (RG027, Beyotime), and Firefly luciferase activity was normalized to *Renilla* luciferase activity.

qRT-PCR analysis

Total RNA was extracted using TRIzol reagent (RK30129) and reverse transcribed using the ABScript III RT Master Mix (RK20429). qRT-PCR was performed with the SYBR Green Fast qPCR Kit (RK21204, ABclonal) on a LineGene 9600 Plus Fluorescence qPCR Detection System (Bioer Technology, Hangzhou, China). GAPDH served as the internal control. Relative mRNA expression was calculated by the $2^{-\Delta\Delta CT}$ method and normalized to the control group [26]. Primers are listed in **Table S1.**

Immunoblotting

Cells were lysed in RIPA buffer (50 mM Tris, 1% Triton X-100, 0.5% sodium deoxycholate, 0.1% SDS, 150 mM NaCl, 10 mM $MgCl_2$ and 5% glycerol, pH 7.2) containing protease inhibitors on ice for 30 min. Lysates were centrifuged at 14, 000 *g* for 15 min at 4°C, and supernatants were collected. Equal protein amounts (20-40 μg) were separated by 6-15% SDS-PAGE, transferred to polyvinylidene difluoride (PVDF) membranes, and blocked with 3% bovine serum albumin (BSA) in TBST. Membranes were incubated with primary antibodies overnight at 4°C, followed by HRP-conjugated secondary antibodies (1:5000; A0216 or A0208, RRID:AB_2860575 or RRID:AB_2892644, Beyotime). Protein signals were visualized with enhanced chemiluminescence (ECL) reagent (Vazyme Biotech; Nanjing, China).

Cell proliferation assay

For EdU assay, cells were treated with 5-ethly-2'-deoxyuridine (EdU, 1:1000) for 12 h, fixed, permeabilized, blocked and stained with iClick™ EdU Andy Fluor™ 647 Flow Cytometry Assay Kit (GeneCopoeia, Rockville, MD, USA) according to the manufacturer's instructions. EdU incorporation was quantified by flow cytometry.

Transwell assay

Cells (3×10^4) suspended in serum-free medium were seeded into 8 μm pore transwell inserts (Jet Biofil, Guangzhou, China), with medium containing 10% FBS in the lower chamber as a chemoattractant. After incubation at 37°C for 36 h, cells were fixed with 4% paraformaldehyde (PFA) and stained with 0.1% crystal violet.

Co-culture model of ECs and immune cells

THP-1 cells were polarized into M0 macrophage by CSF-1 (50 ng/mL; HY-P7050, MCE, USA) for 5 days. Jurkat cells were activated with PMA (50 ng/mL; HY-18739, MCE) and ionomycin (1 μg/mL; Aladdin, Shanghai, China) for 4-6 h. Polarized THP-1 or activated Jurkat cells (1×10^6/well) were overlaid onto and co-cultured for 48 h with a monolayer of ECs that had been seeded at 5×10^5/well in 12-well plates.

Immunoprecipitation

Cells were resuspended in precooled immunoprecipitation lysis buffer (P0013, Beyotime) containing the protease inhibitor cocktail for 30 min on ice. Protein lysates (2 mg) were incubated with 2.5 μg control IgG or an equal amount of anti-ubiquitin or anti-ITGA3 antibody at 4°C for 1 h, followed by overnight incubation with 30 μL protein A/G magnetic beads at 4°C. The immunoprecipitated complexes were then eluted and subjected to immunoblotting analysis.

Isolation of cell-secreted proteins

Cell culture supernatants were collected, supplemented with protease inhibitors, and sequentially centrifuged (500 g, 10 min; 2000 g, 20 min) to remove cells and debris. After filtration through a 0.22 μm filter, samples were concentrated 10-fold using a 10 kDa MWCO filter (Merck Millipore) at 4 °C. Concentrated samples were stored at -80 °C for subsequent immunoblotting or ELISA.

ELISA assay

Cell-secreted proteins or serum samples from BLCA patients were added into 96-well ELISA plates (Jet Biofil, Guangzhou, China) and incubated for 2 h at 37℃, followed by blocked with 1% BSA in PBS. After washing, 100 μL of appropriately diluted primary antibodies were added and incubated overnight at 4°C. Subsequently, 100 μL HRP-conjugated secondary antibody solution was added to each well and incubated for 1 h at 37℃, followed by reaction with 150 μl TMB substrate (P0206, Beyotime) at RT for 30 min. The reaction was terminated with 2 M H_2SO_4, and the optical density was determined at 450 nm by a microplate reader (BioTek Synergy; Winooski, VT, USA).

Immunofluorescence assay

Cells were seeded on Poly-HEMA coated plates for 24 h and cultured for 24 h, then fixed with 4% PFA for 15 min at RT and permeabilized with 0.2% Triton X-100 for 20 min. After blocking with 3% BSA in PBS for 1 h, cells were incubated with primary antibodies overnight at 4°C, followed by Alexa Fluor 488-labeled goat anti-rabbit IgG secondary antibody (A0423, RRID:AB_2891323, Beyotime), DAPI and Phalloidin-

iFluor 647 (ab176759; Abcam, Cambridge, MA, USA). Images were acquired using an inverted fluorescence microscope (Leica, Wetzlar, Germany).

Proteomics analysis

Total cellular proteomics analysis was performed as described in our previous study [18]. Proteins (500 μg) were extracted in lysate buffer (8 M urea, 50 mM NH_4HCO_3), centrifuged at 10, 000 *g* for 15 min, and the supernatant was reduced with DTT and alkylated with IAM. The urea concentration was then diluted to < 1 M before sequential digestion with Lys-C (Wako Puro Chemical; Osaka, Japan) and trypsin (Promega; Madison, WI, USA). Peptides were acidified with 10% trifluoroacetic acid (pH < 2), desalted using Oasis HLB cartridges, and subjected to two-dimensional LC- MS on an LTQ Orbitrap System (RRID:SCR_018701, Thermo Fisher). Data were processed with MaxQuant software (RRID:SCR_014485)e [27].

XF extracellular flux analyzer experiments

The cell mitochondrial stress pretreated with palmitic acid (PA) is as previously reported [28]. Cells were pre-treated with BSA-palmitate (150 μM) for 24 h. The oxygen consumption rate (OCR) was measured using the XF Mito Cell Stress Test (103575-100, Agilent Technologies, Santa Clara, CA, USA) according to the manufacturer's instructions. A total of 1.5×10^4 cells/well were seeded in an XF HS Mini microplate and cultured for 24 h. The sensor cartridge was hydrated overnight and further equilibrated with XF Calibrant for 1 h. Cells were washed with Test solution (Seahorse XF DMEM Medium, pH 7.4 supplemented with 2 mM glutamine, 10 mM glucose, and 1 mM pyruvate) and incubated at 37°C (no CO_2) for 1 h. Drugs were dissolved in Test solution and loaded into the cartridge: 1.5 μM Oligomycin (20 μL in Port A); 2.0 μM FCCP (22 μL in Port B); 0.5 μM Rotenone/antimycin A (25 μL in Port C). The sensor cartridge was calibrated, and then XF HS Mini cell culture microplate was inserted into the instrument for three cycles. Data were normalized by protein content.

Detection of cellular and mitochondria-specific ROS

Mitochondrial ROS levels were assessed using the Mitochondrial Superoxide Assay Kit with MitoSO™ Red (S0061S, Beyotime). Cells were seeded in 6-well plates and incubated with MitoSO™ Red for 1 h at 37°C. Cellular ROS were measured using the DCFH-DA (S0033S, Beyotime). Cells were incubated with DCFH-DA for 30 min at 37°C and counterstained with Hoechst 33342 (Thermo Fisher Scientific). Fluorescence was detected by fluorescence microscopy or flow cytometry.

Animal models

C57BL/6 (RRID:IMSR_JAX:000664) wild-type (WT) mice (5 weeks old) were purchased from Vital River Laboratory Animal Technology (Beijing, China) under specific pathogen-free (SPF) conditions with controlled temperature (22 ± 2 °C) and humidity (50-60%), under a 12 h light/12 h dark cycle, with ad libitum access to standard laboratory chow and water. A total of 2×10^6 cells in 200 μL of PBS were

subcutaneously injected into the right dorsal flank of mice. Tumor growth was monitored for 21 days post-xenografting. Mice were then humanely sacrificed by cervical dislocation, and tumor and spleen tissues were collected for histological analysis and preparation of single-cell suspensions.

Isolation of splenic and peripheral blood lymphocytes

Mouse spleens were aseptically excised and processed using Mouse 1× Lymphocyte Separation Medium (DKW33, DAKEWE, Shenzhen, China). In brief, spleens were gently homogenized through a 70 μm cell strainer into the separation solution, and RPMI 1640 was added slowly onto the cell suspension. For peripheral blood obtained by retro-orbital plexus or cardiac puncture, mice were anesthetized by intraperitoneal injection of tribromoethanol (25 mg/mL, 140 μL per 10 g body weight) prior to blood collection. Blood was diluted 1:1 with sterile 0.9% NaCl and then carefully layered onto the separation solution. All samples were centrifuged at 800 *g* for 30 min at low acceleration and deceleration. Lymphocytes at the interface were collected, washed with RPMI 1640, and resuspended in RPMI 1640 containing 20% FBS for subsequent analyses.

Preparation of single-cell suspension from tumor tissue

Mouse tumors were aseptically excised and transferred at RT in Hanks' Balanced Salt Solution (HBSS) containing Ca^{2+} and Mg^{2+} (C0219, Beyotime). Tissues were minced into 1-2 mm pieces and digested in RPMI 1640 containing 2% FBS, 2 mg/mL collagenase type IV (MX1001), 1 mg/mL Dispase type II (MX1006) and 10 μg/mL DNase I (MF0402; Maokang Biotechnology, Shanghai, China) at 37 °C for 30-60 min with shaking at 180 rpm. Following filtration by a 70 μm strainer into RPMI 1640 medium containing 20% FBS, the cell suspension was centrifuged at 300 *g* for 5 min, and treated with red blood cell lysis buffer for 5 min at RT. Cells were washed twice with 0.85% normal saline and resuspended in RPMI 1640 with 20% FBS to obtain single-cell suspensions for subsequent analyses.

Isolation of tumor-infiltrating lymphocytes

Mononuclear cells from tumor tissues were isolated by Percoll (P8370, Solarbio, Beijing, China) density gradient centrifugation using 80% and 40% Percoll layers with the cell suspension layered on top (400 *g*, 30 min at low acceleration and deceleration). The tumor-infiltrating lymphocytes (TILs) were collected from the interface, washed with 0.85% saline and treated with red blood cell lysis buffer for 5 min at RT. Cells were washed and resuspended in RPMI 1640 containing 20% FBS to obtain TILs for downstream analyses.

Isolation and purification of tumor endothelial cells

Single-cell suspensions from tumor tissues were subjected to magnetic-activated cell sorting (MACS) using CD31 MicroBead Kit (130-097-418, Miltenyi Biotec, Germany) following the manufacturer's protocol. Briefly, cell suspensions were incubated with CD31 MicroBeads at 4 °C for 15 min, washed with MACS buffer (PBS containing 0.5% BSA and 2 mM EDTA), and loaded into MACS separation columns placed in a magnetic field. Unlabeled cells were discarded, and $CD31^+$ cells retained in the column were

eluted after removal from the magnet. Purified TECs were collected and immediately used for further analyses.

Isolation of naïve CD4$^+$T cells from spleens and peripheral blood

Naïve CD4$^+$ T cells were isolated from splenic and peripheral blood lymphocytes using a MagniSort™ Mouse CD4 Naïve T cell Enrichment Kit (8804-6824, Thermo Fisher Scientific) following the manufacturer's instructions. Briefly, lymphocytes were incubated with MagniSort^{TM} Enrichment Antibody Cocktail against non-Naïve CD4$^+$ T cell markers, followed by incubation with the MagniSort^{TM} Negative Selection Beads. Bead-bound cells were removed with a magnetic separation rack, and untouched naïve CD4$^+$ T cells were collected from the supernatant. The isolated naïve CD4$^+$ T cells were confirmed by flow cytometry and subsequently cultured in complete RPMI-1640 medium supplemented with 100 U/mL IL-2 (R&D Systems, USA).

In vitro CD4$^+$ T cell polarization with TECs

CD4$^+$ T cell polarization was performed as previously described [22]. TECs (5×10^4/well) were seeded in the 24-well plates and allowed to adhere overnight. The following day, naïve CD4$^+$ T cells (5×10^5/well) were added and stimulated with Dynabeads® Mouse T-Activator CD3/CD28 (11453D, Thermo Scientific). Th17 differentiation was induced by culturing cells for 5 days in the presence of IL-6 (20 ng/mL; RP01321), TGF-β (1 ng/mL; RP00671), IL-1β (10 ng/mL; RP01340, ABclonal), anti-IFN-γ mAbs (10 μg/mL; #BE0055, RRID:AB_1107694) and anti-IL-4 mAbs (5 μg/mL; #BE0045, RRID:AB_1107707, Bio X cell, USA).

For trans-differentiation, Th17 cells were subsequently re-stimulated for 2 days with either IL-12 (10 ng/mL; Z03211-10, GenScript, Nanjing, China) plus anti-IL-4 mAbs (5 μg/mL; #BE0045, Bioxcell) to promote Th1 conversion, or with TGF-β (5 ng/mL) and IL-2 (100 U/mL) to promote Treg conversion. Differentiation and trans-differentiation were assessed by intracellular cytokine staining and flow cytometry at the indicated time points.

Flow cytometry for immune cell differentiation

Flow cytometry analysis was performed as previously described [22]. In brief, Jurkat or CD4$^+$ T cells were stimulated with PMA and ionomycin in the presence of brefeldin A (10 μg/mL; HY-16592, MCE) for 5 h. Mouse CD4$^+$ T cells were stained with PE-conjugated anti-CD4 mAb (A25933, Abclonal), while THP-1 cells were incubated with FITC anti-human CD14 (301803, RRID:AB_314185) and PE/Cyanine7 anti-human CD163 Antibody (333613, RRID:AB_2562640, Biolegend; San Diego, CA, USA) on ice for 30 min in the dark.

For intracellular cytokine staining, mouse cells were fixed and permeabilized using the Foxp3/Transcription Factor Fixation/Permeabilization Buffer Set (FXP058S, 4A Biotech, Suzhou, China) and stained with following antibodies: APC anti-mouse IL17A (A27628), FITC anti-mouse IFNγ (A27484)

and AF488 anti-mouse Foxp3 (A26228) from Abclonal. Jurkat cells were fixed, permeabilized, blocked, and incubated with primary antibodies against IL17A and Foxp3 (P012685, Epizyme, Shanghai, China) for 2 h at RT, followed by fluorescently-labeled secondary antibodies (AF488 anti-rabbit IgG and AF647 anti-mouse IgG) or AF488 anti-human IFNγ (A25557).

$CD4^+$ T cell subset-mediated tumor killing

Cytotoxic CD4 T cell assessment was performed as previously described [29]. Naïve $CD4^+$ T cells isolated from spleen or TILs were stimulated under Th17-inducing cytokines condition for 5 days and subsequently treated with Brefeldin A to inhibit IL17A secretion. MB49 were labeled with CFSE (5 μM; HY-D0938, MCE) for 30 min at 37°C in the dark and co-culture with Th17 cells at a 1:5 ratio for 24 h. The tumor killing was assessed using Annexin V-APC/7AAD Apoptosis Kit (BioLegend). Apoptotic populations (Annexin $V\text{-}APC^+/7AAD^-$ for early apoptosis; Annexin $V\text{-}APC^+/7\text{-}AAD^+$ for late apoptosis) were analyzed by flow cytometry.

Statistical analysis

Statistical analysis was conducted using GraphPad Prism 8.0 (RRID:SCR_002798, GraphPad software, USA). The results are presented as the means ± standard error of the mean (SEM) from three or more independent experiments. Statistical comparisons between two groups were determined using an unpaired two-tailed Student's t-test. Spearman correlation analysis was performed to evaluate the association between variables that did not follow a normal distribution. A p-value of less than 0.05 was considered to indicate a statistically significant difference.

Results

SLeX glycosylation of ITGA3 drives Endo-MT in ECs

Our previous study demonstrated that sLeX-modified ITGA3 disrupts the vascular barrier and promotes BLCA metastasis through tumor-derived small extracellular vesicles (sEVs) [18]. Since loss of vascular integrity is frequently linked to Endo-MT [30], we next examined whether sLeX-modified ITGA3 drives Endo-MT in ECs.

Overexpression of wild-type ITGA3 (ITGA3_HA) significantly increased HUVECs proliferation relative to vector controls (Vector), whereas sLeX glycosylation- deficient mutant (N265A_HA) showed markedly reduced proliferation **(Figure S1A)**. Consistently, ITGA3_HA cells displayed enhanced migratory capacity, whereas N265A_HA cells showed impaired migration relative to ITGA3_HA group **(Figure 1A)**. ITGA3_HA cells exhibited reduced expression of endothelial markers (VE-Cadherin, CD31 and vWF) and elevated expression of mesenchymal markers (Fibronectin, α-SMA, and Vimentin), relative to Vector and N265A_HA groups **(Figure 1B)**. These results suggest that sLeX-modified ITGA3 promotes a mesenchymal-like phenotype in ECs. We further assessed the expression of key transcription factors (TFs) implicated in EMT, including Snail1, Slug, and Twist1 [31-33]. Among these, only Slug was

significantly upregulated in ITGA3_HA cells compared with the other two groups **(Figure 1C)**. Consistently, qRT-PCR analyses confirmed that ITGA3_HA cells exhibited gene expression patterns characteristic of Endo-MT **(Figure 1D&E)**.

Slug is known to repress epithelial gene expression by binding to E-box motifs in promoter regions, such as *CDH1* (E-Cadherin) [34]. Given the evolutionary homology within the cadherin family and the conservation of E-box motifs across cadherin promoters, we next examined whether Slug also targets the *CDH5* (VE-Cadherin) promoter. Twenty E-box motifs were identified in the *CDH5* promoter, among which EB4 (-2566 bp), EB11 (-1258 bp) and EB17 (-373 bp) were predicted as potential Slug-binding regions based on previous reports and AlphaFold3 modeling **(Figure 1F)** [35]. Overexpression of wild-type ITGA3 augmented Slug-mediated repression of *CDH5*, whereas the effect was attenuated by the N265A mutation in both HEK-293T and HUVECs **(Figure S1B, 1G&H)**. Reporter assays using single and triple E-box mutants revealed progressively reduced in Slug activity, with the triple mutant exhibiting the most pronounced loss **(Figure 1I&J)**. Consistently, ChIP-qPCR confirmed increased Slug occupancy at these E-boxes in the presence of sLeX-glycosylated ITGA3, but not in Vector or N265A mutants **(Figure S1C, 1K)**. These findings indicate that sLeX modification of ITGA3 enhances Slug recruitment to the *CDH5* promoter, leading to VE-Cadherin repression and Endo-MT induction in TECs.

SLeX-modified ITGA3 stabilizes Slug via EGFR-AKT-GSK3β

Using an in-depth analysis of our previously published proteomics data [18], we found that sLeX-modified ITGA3 exhibited enrichment of proteins associated with the ERBB signaling pathway, which is mediated by receptor tyrosine kinases of the EGFR family **(Figure S1D)**. Consistent with reports that integrin α3β1 activates ERBB signaling in NSCLC [36], AlphaFold3-based structural prediction showed that N-glycosylation at Asn265 altered the local conformation of ITGA3, potentially facilitating its interaction with the β1 I-like domain. **(Figure 2A&B)**. Experimentally, this glycosylation enhanced heterodimerization between ITGA3 and ITGB1 without affecting ITGB1 expression **(Figure 2C&D)**.

SLeX glycosylation of ITGA3 markedly activated the ERBB signaling cascade, as evidenced by increased phosphorylation of EGFR and AKT, accompanied by reduced phosphorylation of GSK3β at Tyr216, a site required for its activation, indicative of decreased GSK3β activity [37]. Conversely, the loss of sLeX glycosylation diminished α3β1 complex formation, attenuated ERBB signaling, and increased GSK3β activity **(Figure 2E)**. Given that GSK3β activation promotes β-TrCP–mediated ubiquitination and degradation of EMT-associated TFs [32], Slug protein was significantly more stable in ITGA3_HA cells compared to the N265A_HA cells **(Figure 2F)**. Accordingly, Slug in ITGA3_HA cells showed markedly reduced association with β-TrCP and decreased ubiquitination, whereas N265A_HA cells exhibited enhanced β-TrCP binding, increased Slug ubiquitination, and diminished nuclear accumulation **(Figure 2G&H)**. Taken together, sLeX-modified ITGA3 stabilizes Slug by strengthening integrin α3β1 heterodimerization and activating ERBB–AKT signaling to inhibit GSK3β, thereby reducing Slug ubiquitination, preventing its degradation, and sustaining its nuclear accumulation to drive Endo-MT.

SLeX-ITGA3 in HUVECs reprograms Th17 differentiation

As FUT7 is the key rate-limiting enzyme for sLeX synthesis, co-expression analysis using the BLCA dataset (TCGA, Cell 2017) revealed that FUT7-associated genes were significantly enriched in immune-related pathways, particularly T cell receptor signaling and Th17 differentiation **(Figure 3A&B; Table S2)**. Analysis of UALCAN data showed that IL17A, a canonical Th17 effector molecule, was markedly reduced in late-stage BLCA and its low expression predicted poor survival **(Figure S2A&B)**.

To examine whether TECs influence Th17 differentiation in the BLCA microenvironment, Jurkat cells (a human $CD4^+$ T cell leukemia line) were co-cultured with indicated ECs **(Figure 3C)**. ITGA3_HA cells markedly suppressed conventional Th17 differentiation relative to Vector and N265A_HA, as indicated by reduced IL17A secretion and downregulated Th17-associated transcription factors STAT3 and RORγt **(Figure 3D-F).**

Because cytokines critically shape Th17 fate decisions **(Figure 3G)**, we next evaluated the major cytokines. Intriguingly, ITGA3_HA ECs produced significantly higher levels of TGFβ despite exhibiting markedly reduced IL1β/IL6 **(Figure 3H&I)**. As TGFβ functions in a concentration-dependent manner, with low levels supporting Th17 differentiation and high levels driving Th17 cells toward a Treg-like state, the pattern suggests that ITGA3_HA ECs may not only inhibit classical Th17 differentiation but also modulate Th17 plasticity [38]. Th17 can mainly trans-differentiate into Th1-like or Treg-like subsets depending on the cytokine milieu [38, 39]. Thus, IFNγ (a Th1-associated marker) and Foxp3 (a Treg-associated marker) expression was assessed. Jurkat cells co-cultured with ITGA3_HA expressed higher levels of Foxp3 but not IFNγ relative to those co-cultured with N265A_HA **(Figure 3E&F)**. ITGA3_HA cells reduced the proportion of $IFN\gamma^+IL17A^+$ (Th1-like Th17) cells, while increasing $Foxp3^+IL17A^+$ (Treg-like Th17) cells compared to N265A_HA group **(Figure 3J&K)**. Additionally, the polarization of M2 macrophages, as the one of essential immune cells in tumor environment, was not directly regulated by indicated ECs **(Figure S2C)**.

Consistently, serum IL17A levels were reduced in BLCA patients compared with healthy controls (HC) **(Figure 3L)**. IL1β and IL6 were also decreased, whereas TGFβ was elevated in patients **(Figure 3M)**, with IL17A correlating positively with IL1β/IL6, but not TGFβ **(Figure 3N)**. Collectively, these results demonstrate that sLeX-modified ITGA3 in ECs suppresses conventional Th17 differentiation and promotes a Treg-like Th17 phenotype, likely via altered cytokine secretion and Endo-MT-associated signals in tumor endothelium.

Enhanced sLeX glycosylation attenuates Th1-like Th17 responses in vivo

Using mouse xenograft models, we further examined $CD4^+$ T cell differentiation in peripheral blood, tumor tissues, and spleen from MB_WT (wild-type MB49), MB_sg (FUT7-sgRNA), and MB_OE (FUT7-overexpression) tumor-bearing mice **(Figure S3A, 4A)**. In the peripheral blood, the proportions of Th17, Th1-like Th17 ($IFN\gamma^+IL17A^+CD4^+$), and conventional Th1 ($IFN\gamma^+CD4^+$) cells were highest in MB_sg mice and lowest in MB_OE mice. Conversely, Treg-like Th17 ($Foxp3^+IL17A^+CD4^+$) and conventional Treg ($Foxp3^+CD4^+$) cells exhibited the opposite pattern, being enriched in MB_OE and reduced in MB_sg mice **(Figure 4B-D, H)**. Analysis of TILs and spleen revealed a similar trend: Th17, Th1-like Th17, and Th1 cells

were markedly suppressed in MB_OE tumors, whereas Treg-like Th17 and Treg cells were increased, suggesting sLeX upregulation shapes $CD4^+$ T cell differentiation and may alter their trafficking among peripheral lymphoid organs **(Figure 4E-G, I, S4B-D)**. Collectively, these findings demonstrate that enhanced sLeX glycosylation suppresses Th1-like Th17 differentiation while promoting Treg-like Th17 differentiation in vivo.

Considering the stronger cytotoxic activity and antitumor properties of Th1-like Th17 subset [22], naïve $CD4^+$ T cells were isolated from spleen and peripheral blood of MB_sg, MB_WT, and MB49_OE mice, differentiated into Th17 cells in vitro, and subsequently co-cultured with MB49 cells **(Figure 5A)**. MB49 cells exhibited significantly higher apoptosis when co-cultured with Th17 cells derived from MB_sg mice, whereas the cytotoxic activity of Th17 cells from MB_OE mice was markedly attenuated **(Figure 5B-E)**. These findings indicate that elevated sLeX levels suppress Th17-to-Th1 trans-differentiation, thereby facilitating tumor immune escape.

To further determine the contribution of TECs to Th17 fate decisions, TECs were isolated from each group of tumors and co-cultured with naïve $CD4^+$ T cells **(Figure S3E)**. TECs from MB_sg mice increased the proportions of Th17 and Th1-like Th17 cells while reducing Treg-like Th17 cells, whereas MB_OE TECs exerted the opposite effects **(Figure 5F-H)**. Under Th1-differentiating conditions, MB_sg TECs enhanced Th17-derived Th1 conversion, while they suppressed Th17-derived Treg formation under Treg conditions; the MB_OE TECs again showed inverse effects **(Figure 5I-K)**. Taken together, these findings demonstrate that TECs in BLCA with high sLeX expression suppress Th17 and Th17-derived Th1 differentiation while promoting Th17-derived Treg generation, thereby contributing to an immunosuppressive TME.

FALDH-mediated FAO enhances endothelial promotion of Th17 differentiation

Proteomic data revealed ITGA3_HA cells exhibited lower enrichment of fatty acid (FA) metabolism-related pathways compared with N265A_HA cells **(Figure 6A; Table S3&4)**. Among the differentially expressed proteins, FALDH, an enzyme catalyzing the oxidation of medium- and long-chain aliphatic aldehydes into FA, was notably reduced in ITGA3_HA **(Figure 6B)**. Given previous reports that FAO maintains vascular integrity by limiting Endo-MT [40], and considering the potential reduction of FA substrates upon FALDH loss, we reasoned that altered FAO might underlie the distinct immunomodulatory properties of these ECs **(Figure 6C)**.

Consistently, ITGA3_HA cells exhibited reduced expression of FALDH and CPT1A, a rate-limiting enzyme that catalyzes the transport of long-chain FA into mitochondria for FAO, while PPARα, the upstream transcriptional regulator of CPT1A, remained unchanged **(Figure 6D)**, implying a possible PPARα-independent mechanism regulating CPT1A under sLeX-modified ITGA3. FAO activity was impaired in ITGA3_HA cells, as indicated by diminished OCR following palmitic acid (PA) supplementation **(Figure 6E)**. Given that FAO can dynamically regulate oxidative stress, which in turn modulates pro-inflammatory cytokine production **(Figure 6C)** [41, 42], ROS levels were examined. Both total and mitochondrial ROS were reduced in ITGA3_HA cells compared to N265A_HA cells **(Figure 6F&G, S4A&B)**, supporting the

notion that sLeX-modified ITGA3 may suppress FALDH-mediated FAO, which in turn reduces ROS production and alters cytokine secretion.

FALDH overexpression in ITGA3_HA cells (FALDH OE) restored CPT1A expression and OCR, elevated cellular and mitochondrial ROS, and promoted IL1β/IL6 secretion but reduced TGFβ, ultimately enhancing the frequency of total IL17A$^+$ cells in Jurkat and upregulating p-STAT3 and RORγt expression **(Figure 6H-K, S4C-F S5A-C)**. Conversely, FALDH knockout in N265A_HA cells reduced CPT1A expression and OCR, lowered ROS levels, and decreased IL1β/IL6 secretion, and impaired total IL17A$^+$ cells in Jurakt **(Figure 6L-O, S4G-J, S5G-J)**.

Functionally, FALDH OE cells favored Th1-like Th17 differentiation, while reducing Treg-like Th17 cells, accompanied by increased IL17A and IFNγ secretion **(Figure 6P, Q, S and S5B&C)**. In contrast, FALDH KO diminished Th1-like Th17 subsets and promoted Treg-like Th17 cells **(Figure 6R&S, S5I&J)**. Together, these findings indicate that low FALDH expression in ITGA3_HA ECs reduces CPT1A-dependent FAO, leading to decreased ROS and attenuated pro-inflammatory cytokine secretion, ultimately skewing Th17 differentiation toward a regulatory rather than inflammatory phenotype.

Endothelial FAO regulated by EGFR-AMPK axis guides Th17 differentiation

AMP-activated protein kinase (AMPK) is a central metabolic sensor that promotes FAO to maintain energy balance [43]. ITGA3_HA cells showed markedly reduced AMPK phosphorylation compared with Vector and N265A_HA, consistently indicating suppressed FAO activity **(Figure S6A)**. Considering that dysfunctional FAO in ECs can trigger Endo-MT involving ERBB signaling, N265A_HA cells were treated with the CPT1A inhibitor Etomoxir, which indeed activated EGFR/AKT signaling **(Figure 7A)**. Consistent with the reported mutual antagonism between ERBB and AMPK pathways [44], FAO inhibition further reduced AMPK phosphorylation and CPT1A expression, while FALDH and PPARα remained unchanged **(Figure 7A&B)**. These data indicate that sLeX-modified ITGA3 represses endothelial FAO via an AMPK-EGFR/AKT negative feedback loop.

Functionally, FAO blockade in N265A_HA cells suppressed IL1β/IL6 secretion but increased TGFβ, leading to reduced Th17/Th1 markers and elevated Foxp3 expression in co-cultured Jurkat (**Figure 7C-G, S6B)**. Accordingly, the frequencies of IL17A$^+$ and IL17A$^+$IFNγ$^+$ cells were decreased, whereas Foxp3$^+$IL17A$^+$ subsets were increased **(Figure 7H)**.

Conversely, inhibiting EGFR in Endo-MT–like ITGA3_HA cells with AG1478 suppressed EGFR/AKT phosphorylation and restored AMPK activity, accompanied by recovery of FAO-related proteins FALDH and CPT1A but not PPARα **(Figure 7I&J)**. In parallel, EGFR inhibition restored pro-inflammatory cytokine secretion, suppressed TGFβ, and increased IL17A$^+$ and IL17A$^+$IFNγ$^+$ Jurkat while reducing Foxp3$^+$ cells, consistent with enhanced Th17/Th1 marker expression and Foxp3 repression **(Figure 7K-P, S6C).** Likewise, FALDH overexpression reduced ERBB activity and enhanced AMPK phosphorylation, whereas FALDH knockout produced the opposite effect **(Figure S6D&E)**. In summary, these findings demonstrate that sLeX-glycosylated ITGA3 activates EGFR/AKT signaling to suppress AMPK-driven FAO

through FALDH downregulation, forming an ERBB-AMPK double-negative feedback loop that limits endothelial support for Th17 differentiation and Th17-to-Th1 trans-differentiation.

Discussion

The TME constitutes a complex and multicellular milieu that fosters cancer progression. Angiogenesis within the TME is orchestrated by a dynamic interplay of signaling molecules and pathways, involving EC proliferation, migration, and morphogenesis. Beyond serving as passive conduits for blood supply, TECs are increasingly recognized as active players in shaping the tumor niche. Through dynamic crosstalk with cancer cells, stromal cells and infiltrating immune cells, TECs not only sustain aberrant angiogenesis but also influence vascular permeability, immune cell trafficking and the overall immunosuppressive landscape of the TME [45]. However, TEC-intrinsic glycosylation in immune regulation remains poorly characterized.

Increasing evidence indicates that ECs exhibit remarkable phenotypic plasticity and can undergo Endo-MT, a process analogous to EMT, whereby ECs lose endothelial markers and acquire a mesenchymal phenotype [46]. Compared with EMT, Endo-MT in cancer remains less well characterized, as most studies linking ECs to cancer have primarily focused on tumor angiogenesis as a prerequisite for tumor growth and metastasis [47]. Recent findings reveal that tumor ECs can undergo Endo-MT to drive Snail/Slug-dependent aberrant vascularization [11]. Mechanistically, members of the Snail family are predominantly degraded via β-TrCP-mediated ubiquitination triggered by active GSK3β, whose activity is negatively regulated by ERBB-PI3K-AKT signaling [48]. Notably, Slug appears to play a more prominent role in BLCA than other transcriptional repressors [49]. Building on these concepts, we propose that sLeX-modified ITGA3 heterodimerizes with ITGB1, activating EGFR/AKT to inhibit GSK3β, thereby stabilizing nuclear Slug, repressing VE-Cadherin transcription, and driving Endo-MT in TECs.

The tumor endothelium has traditionally been viewed as an angiogenic element and largely passive physical barrier, preventing T cell extravasation and thereby impairing anti-tumor immunity through T cell anergy [4]. However, emerging evidence indicates that it can also act as an active immune regulator to directly suppress T cell responses [50]. For instance, sinusoidal ECs of murine liver suppress Th1 and Th17 effector $CD4^+$ T cell activity through via IL10 and PD-1 mediated signaling [51].-Among $CD4^+$ T cells, Th17 cells are abundant in many TME, yet their role in cancer remains controversial due to their plasticity with Treg or Th1 cells. In muscle-invasive bladder cancer (MIBC), the neuronal subtype, associated with higher malignancy, exhibits the lowest Th17 abundance, whereas the luminal papillary (LP) subtype, linked to lower malignancy, shows higher Th17 infiltration [52]. These findings are consistent with our previous observation that sLeX-modified ITGA3 is more efficiently transferred into TECs via small extracellular vesicles from MIBC cells than from non-muscle-invasive bladder cancer (NMIBC) cells. Notably, similar to Th1 and cytotoxic $CD4^+$ T cells, Th17 cells have been shown to exert anti-tumor effects in $PD\text{-}L1^+$ BLCA [53], and $IL\text{-}17A^+$ tumor-infiltrating cells correlate with enhanced anti-tumor immunity in MIBC [54]. In line with these observations, our study demonstrates that sLeX-modified

ITGA3 in TECs suppresses Th17 differentiation and shifts $CD4^+$ T cell fate toward regulatory phenotypes by reducing IL1β and IL6 secretion, thereby shaping the local immunosuppression microenvironment.

As a hallmark of cancer, metabolic reprogramming supports the energetic demands of tumor cells. However, other cellular components of the TME, including TECs, must also adapt their metabolism during tumorigenesis [55]. By reshaping their metabolic state, TECs regulate not only the transport of essential nutrients but also the adaptability of infiltrating immune cells [56]. Although glycolysis contributes to ~85% of ATP production in ECs, FAO plays indispensable roles in endothelial homeostasis, including barrier integrity and the Endo-MT process [57]. For instance, endothelial loss of CPT1A, a key regulator of FAO, induces EC dysfunction characterized by leukocyte infiltration and barrier disruption [58], while reduced FAO has been shown to accompany Endo-MT [40]. In this context, our data revealed that sLeX modification of ITGA3 reduced FAO activity in ECs, in parallel with Endo-MT induction. Through proteomics profiling, we identified FALDH, a cytoplasmic dehydrogenase catalyzing fatty acid ω-oxidation, feeding products into β-oxidation for energy production [59]. We observed lower FALDH expression in ITGA3_HA cells compared with N265A_HA cells, mediated via EGFR-AKT-AMPK signaling, thereby contributing to FAO suppression. This reduction in FAO creates a downstream cascade: lower FAO limits mitochondrial ROS production, which in turn dampens inflammasome activity and proinflammatory cytokine release. Intriguingly, studies in astrocytes indicate that FAO is essential to maintain mitochondrial ROS formation [60], which are essential for sustaining inflammasome activation and proinflammatory cytokine production. Indeed, mitochondrial ROS promote IL1β expression through inflammasome activity and enhance IL6 production by sustaining JNK–p38 phosphorylation following MAPK phosphatase inactivation [41, 42]. Consistently, decreased FAO in ITGA3_HA cells led to lower ROS, reduced IL1β and IL-6 secretion, and consequently impaired Th17 differentiation and Th1-like Th17 trans-differentiation.

In summary, our study identifies sLeX-glycosylated ITGA3 in TECs as a driver of Endo-MT through activation of the ERBB-GSK3β axis, which stabilizes Slug and represses *CDH5* transcription. This phenotypic shift is coupled to downregulation of FALDH and impaired FAO, leading to diminished mitochondrial ROS. Reduced ROS attenuates pro-inflammatory cytokine production, such as IL1β and IL6. Consequently, the tumor immune microenvironment exhibits an increased proportion of Treg/Th17 cells and a decreased proportion of Th1/Th17 cells, ultimately facilitating immune evasion by tumor cells. Collectively, these findings uncover a novel link between endothelial glycosylation, metabolic reprogramming, and immune suppression in the TME, highlighting FAO or ERBB-AMPK signaling in TECs as potential therapeutic targets to improve anti-tumor immunity.

Declarations

Acknowledgements

This work was supported by the National Natural Science Foundation of China (No. 32371336 and 82172828), Science Foundation for Distinguished Young Scholars of Shaanxi Province (No. 2021JC-39),

Shaanxi Innovation Team Project (No. 2023-CX-TD-58). The authors would like to thank Dr. Liang Liang (The First Affiliated Hospital of Xi'an Jiaotong University) and Dr. Qian Deng (Shaanxi Provincial People's Hospital) for providing clinical resources.

Author contributions

HF conceived and designed the study, performed the experiments, analyzed the data, and wrote the original draft of the manuscript. **HZ** performed the experiments. **FG** provided comments, acquired funding, and reviewed and edited the manuscript. All authors read and approved the final manuscript.

Competing interests

The authors declare that they have no conflict of interest.

Ethics approval

Ethical approval for this study was conducted by the Ethics Committee of the Research Department at Northwest University (Approval No. 230306004). The study was conducted in accordance with the ethical principles outlined in the Declaration of Helsinki. All participants were informed about the purpose of the study, assured of confidentiality, and provided written consent prior to participation. Participation was voluntary, and respondents could withdraw at any time without consequence. All animal experiments were performed in accordance with the guidelines of the Animal Care and Use Committee of Northwest University.

References

1. Chen DS, Mellman I. Oncology meets immunology: the cancer-immunity cycle. Immunity. 2013;39:1-10.
2. Binnewies M, Roberts EW, Kersten K, Chan V, Fearon DF, Merad M, et al. Understanding the tumor immune microenvironment (TIME) for effective therapy. Nat Med. 2018;24:541-50.
3. Hinshaw DC, Shevde LA. The Tumor Microenvironment Innately Modulates Cancer Progression. Cancer Res. 2019;79:4557-66.
4. Schaaf MB, Garg AD, Agostinis P. Defining the role of the tumor vasculature in antitumor immunity and immunotherapy. Cell Death Dis. 2018;9:115.
5. Gkountidi AO, Garnier L, Dubrot J, Angelillo J, Harlé G, Brighouse D, et al. MHC Class II Antigen Presentation by Lymphatic Endothelial Cells in Tumors Promotes Intratumoral Regulatory T cell-Suppressive Functions. Cancer Immunol Res. 2021;9:748-64.
6. Lambrechts D, Wauters E, Boeckx B, Aibar S, Nittner D, Burton O, et al. Phenotype molding of stromal cells in the lung tumor microenvironment. Nat Med. 2018;24:1277-89.
7. Lu Y, Liu Y, Zuo X, Li G, Wang J, Liu J, et al. CXCL12(+) tumor-associated endothelial cells promote immune resistance in hepatocellular carcinoma. J Hepatol. 2025;82:634-48.

8. Solimando AG, Summa S, Vacca A, Ribatti D. Cancer-Associated Angiogenesis: The Endothelial Cell as a Checkpoint for Immunological Patrolling. Cancers (Basel). 2020;12:3380.
9. Fang J, Lu Y, Zheng J, Jiang X, Shen H, Shang X, et al. Exploring the crosstalk between endothelial cells, immune cells, and immune checkpoints in the tumor microenvironment: new insights and therapeutic implications. Cell Death Dis. 2023;14:586.
10. Wang Q, He Z, Huang M, Liu T, Wang Y, Xu H, et al. Vascular niche IL-6 induces alternative macrophage activation in glioblastoma through HIF-2α. Nat Commun. 2018;9:559.
11. Ma W, Wang Y, Zhang R, Yang F, Zhang D, Huang M, et al. Targeting PAK4 to reprogram the vascular microenvironment and improve CAR-T immunotherapy for glioblastoma. Nat Cancer. 2021;2:83-97.
12. Yang F, Akhtar MN, Zhang D, El-Mayta R, Shin J, Dorsey JF, et al. An immunosuppressive vascular niche drives macrophage polarization and immunotherapy resistance in glioblastoma. Sci Adv. 2024;10:eadj4678.
13. Zeisberg EM, Potenta S, Xie L, Zeisberg M, Kalluri R. Discovery of endothelial to mesenchymal transition as a source for carcinoma-associated fibroblasts. Cancer Res. 2007;67:10123-8.
14. Yang F, Lee G, Fan Y. Navigating tumor angiogenesis: therapeutic perspectives and myeloid cell regulation mechanism. Angiogenesis. 2024;27:333-49.
15. Shi SM, Suh RJ, Shon DJ, Garcia FJ, Buff JK, Atkins M, et al. Glycocalyx dysregulation impairs blood-brain barrier in ageing and disease. Nature. 2025;639:985-94.
16. Kasper DM, Hintzen J, Wu Y, Ghersi JJ, Mandl HK, Salinas KE, et al. The N-glycome regulates the endothelial-to-hematopoietic transition. Science. 2020;370:1186-91.
17. Ding M, Shi R, Du Y, Chang P, Gao T, De D, et al. O-GlcNAcylation-mediated endothelial metabolic memory contributes to cardiac damage via small extracellular vesicles. Cell Metab. 2025;37:1344-63.e6.
18. Feng H, Liang L, Deng W, Gao J, Li X, Guan F. Sialyl Lewis X decorated integrin α3 on small extracellular vesicles promotes metastasis of bladder cancer via enhancing vascular permeability. Angiogenesis. 2024;27:883-901.
19. Saini P, Mirji G, Islam SMS, Simons LM, Bhat SA, Bonfanti AP, et al. Targeting Interactions Between Siglec-10 and α3β1 Integrin Enhances Macrophage-Mediated Phagocytosis of Pancreatic Cancer. Cancer Res. 2026;86:99-115.
20. Zou W, Restifo NP. T(H)17 cells in tumour immunity and immunotherapy. Nat Rev Immunol. 2010;10:248-56.
21. Muranski P, Restifo NP. Does IL-17 promote tumor growth? Blood. 2009;114:231-2.
22. Lei X, Xiao R, Chen Z, Ren J, Zhao W, Tang W, et al. Augmenting antitumor efficacy of Th17-derived Th1 cells through IFN-γ-induced type I interferon response network via IRF7. Proc Natl Acad Sci USA. 2024;121:e2412120121.
23. Muranski P, Restifo NP. Essentials of Th17 cell commitment and plasticity. Blood. 2013;121:2402-14.

24. Karpisheh V, Ahmadi M, Abbaszadeh-Goudarzi K, Mohammadpour Saray M, Barshidi A, Mohammadi H, et al. The role of Th17 cells in the pathogenesis and treatment of breast cancer. Cancer Cell Int. 2022;22:108.
25. Li X, Peng X, Zhang C, Bai X, Li Y, Chen G, et al. Bladder Cancer-Derived Small Extracellular Vesicles Promote Tumor Angiogenesis by Inducing HBP-Related Metabolic Reprogramming and SerRS O-GlcNAcylation in Endothelial Cells. Adv Sci (Weinh). 2022;9:e2202993.
26. Schmittgen TD, Livak KJ. Analyzing real-time PCR data by the comparative C(T) method. Nat Protoc. 2008;3:1101-8.
27. Tyanova S, Temu T, Cox J. The MaxQuant computational platform for mass spectrometry-based shotgun proteomics. Nat Protoc. 2016;11:2301-19.
28. Mascaraque M, Courtois S, Royo-García A, Barneda D, Stoian AM, Villaoslada I, et al. Fatty acid oxidation is critical for the tumorigenic potential and chemoresistance of pancreatic cancer stem cells. J Transl Med. 2024;22:797.
29. Agarwal S, Hanauer JDS, Frank AM, Riechert V, Thalheimer FB, Buchholz CJ. In Vivo Generation of CAR T Cells Selectively in Human CD4(+) Lymphocytes. Mol Ther. 2020;28:1783-94.
30. Wei WF, Zhou HL, Chen PY, Huang XL, Huang L, Liang LJ, et al. Cancer-associated fibroblast-derived PAI-1 promotes lymphatic metastasis via the induction of EndoMT in lymphatic endothelial cells. J Exp Clin Cancer Res. 2023;42:160.
31. Yang J, Mani SA, Donaher JL, Ramaswamy S, Itzykson RA, Come C, et al. Twist, a master regulator of morphogenesis, plays an essential role in tumor metastasis. Cell. 2004;117:927-39.
32. Zhou BP, Deng J, Xia W, Xu J, Li YM, Gunduz M, et al. Dual regulation of Snail by GSK-3beta-mediated phosphorylation in control of epithelial-mesenchymal transition. Nat Cell Biol. 2004;6:931-40.
33. Moreno-Bueno G, Cubillo E, Sarrió D, Peinado H, Rodríguez-Pinilla SM, Villa S, et al. Genetic profiling of epithelial cells expressing E-cadherin repressors reveals a distinct role for Snail, Slug, and E47 factors in epithelial-mesenchymal transition. Cancer Res. 2006;66:9543-56.
34. Ye Y, Xiao Y, Wang W, Yearsley K, Gao JX, Shetuni B, et al. ERalpha signaling through slug regulates E-cadherin and EMT. Oncogene. 2010;29:1451-62.
35. Lopez D, Niu G, Huber P, Carter WB. Tumor-induced upregulation of Twist, Snail, and Slug represses the activity of the human VE-cadherin promoter. Arch Biochem Biophys. 2009;482:77-82.
36. Zhu J, Cai T, Zhou J, Du W, Zeng Y, Liu T, et al. CD151 drives cancer progression depending on integrin α3β1 through EGFR signaling in non-small cell lung cancer. J Exp Clin Cancer Res. 2021;40:192.
37. Krishnankutty A, Kimura T, Saito T, Aoyagi K, Asada A, Takahashi SI, et al. In vivo regulation of glycogen synthase kinase 3β activity in neurons and brains. Sci Rep. 2017;7:8602.
38. Wang J, Zhao X, Wan YY. Intricacies of TGF-β signaling in Treg and Th17 cell biology. Cell Mol Immunol. 2023;20:1002-22.

39. Lee YK, Turner H, Maynard CL, Oliver JR, Chen D, Elson CO, et al. Late developmental plasticity in the T helper 17 lineage. Immunity. 2009;30:92-107.
40. Xiong J, Kawagishi H, Yan Y, Liu J, Wells QS, Edmunds LR, et al. A Metabolic Basis for Endothelial-to-Mesenchymal Transition. Mol Cell. 2018;69:689-98.e7.
41. Bulua AC, Simon A, Maddipati R, Pelletier M, Park H, Kim KY, et al. Mitochondrial reactive oxygen species promote production of proinflammatory cytokines and are elevated in TNFR1-associated periodic syndrome (TRAPS). J Exp Med. 2011;208:519-33.
42. Zhou R, Yazdi AS, Menu P, Tschopp J. A role for mitochondria in NLRP3 inflammasome activation. Nature. 2011;469:221-5.
43. Hardie DG, Pan DA. Regulation of fatty acid synthesis and oxidation by the AMP-activated protein kinase. Biochem Soc Trans. 2002;30:1064-70.
44. Saha M, Kumar S, Bukhari S, Balaji SA, Kumar P, Hindupur SK, et al. AMPK-Akt Double-Negative Feedback Loop in Breast Cancer Cells Regulates Their Adaptation to Matrix Deprivation. Cancer Res. 2018;78:1497-510.
45. Cleveland AH, Fan Y. Reprogramming endothelial cells to empower cancer immunotherapy. Trends Mol Med. 2024;30:126-35.
46. Hernández-Camarero P, Toledo B, Diaz-Ruano AB, González-Titos A, García-Ortega MB, Perán M. What is the Impact of Endothelial-to-Mesenchymal Transition in Solid Tumours: A Qualitative Systematic Review and Quantitative Meta-Analysis. Int J Biol Sci. 2025;21:2155-78.
47. Li X, Wang C, Zhang H, Li Y, Hou D, Liu D, et al. circFNDC3B Accelerates Vasculature Formation and Metastasis in Oral Squamous Cell Carcinoma. Cancer Res. 2023;83:1459-75.
48. Nagai Y, Tsuchiya H, Runkle EA, Young PD, Ji MQ, Norton L, et al. Disabling of the erbB Pathway Followed by IFN-γ Modifies Phenotype and Enhances Genotoxic Eradication of Breast Tumors. Cell Rep. 2015;12:2049-59.
49. Kaufhold S, Bonavida B. Central role of Snail1 in the regulation of EMT and resistance in cancer: a target for therapeutic intervention. J Exp Clin Cancer Res. 2014;33:62.
50. Motz GT, Santoro SP, Wang LP, Garrabrant T, Lastra RR, Hagemann IS, et al. Tumor endothelium FasL establishes a selective immune barrier promoting tolerance in tumors. Nat Med. 2014;20:607-15.
51. Carambia A, Frenzel C, Bruns OT, Schwinge D, Reimer R, Hohenberg H, et al. Inhibition of inflammatory CD4 T cell activity by murine liver sinusoidal endothelial cells. J Hepatol. 2013;58:112-8.
52. Vidotto T, Nersesian S, Graham C, Siemens DR, Koti M. DNA damage repair gene mutations and their association with tumor immune regulatory gene expression in muscle invasive bladder cancer subtypes. J Immunother Cancer. 2019;7:148.
53. Wu J, Abraham SN. The Roles of T cells in Bladder Pathologies. Trends Immunol. 2021;42:248-60.
54. Wang Z, Zhou Q, Zeng H, Zhang H, Liu Z, Huang Q, et al. Tumor-infiltrating IL-17A(+) cells determine favorable prognosis and adjuvant chemotherapeutic response in muscle-invasive bladder cancer.

Oncoimmunology. 2020;9:1747332.
55. García-Caballero M, Sokol L, Cuypers A, Carmeliet P. Metabolic Reprogramming in Tumor Endothelial Cells. Int J Mol Sci. 2022;23:11052.
56. Kane K, Edwards D, Chen J. The influence of endothelial metabolic reprogramming on the tumor microenvironment. Oncogene. 2025;44:51-63.
57. De Bock K, Georgiadou M, Schoors S, Kuchnio A, Wong BW, Cantelmo AR, et al. Role of PFKFB3-driven glycolysis in vessel sprouting. Cell. 2013;154:651-63.
58. Kalucka J, Bierhansl L, Conchinha NV, Missiaen R, Elia I, Brüning U, et al. Quiescent Endothelial Cells Upregulate Fatty Acid β-Oxidation for Vasculoprotection via Redox Homeostasis. Cell Metab. 2018;28:881-94.e13.
59. Sasaki Y, Raza-Iqbal S, Tanaka T, Murakami K, Anai M, Osawa T, et al. Gene Expression Profiles Induced by a Novel Selective Peroxisome Proliferator-Activated Receptor α Modulator (SPPARMα) Pemafibrate. Int J Mol Sci. 2019;20:5682.
60. Morant-Ferrando B, Jimenez-Blasco D, Alonso-Batan P, Agulla J, Lapresa R, Garcia-Rodriguez D, et al. Fatty acid oxidation organizes mitochondrial supercomplexes to sustain astrocytic ROS and cognition. Nat Metab. 2023;5:1290-302.

Figures

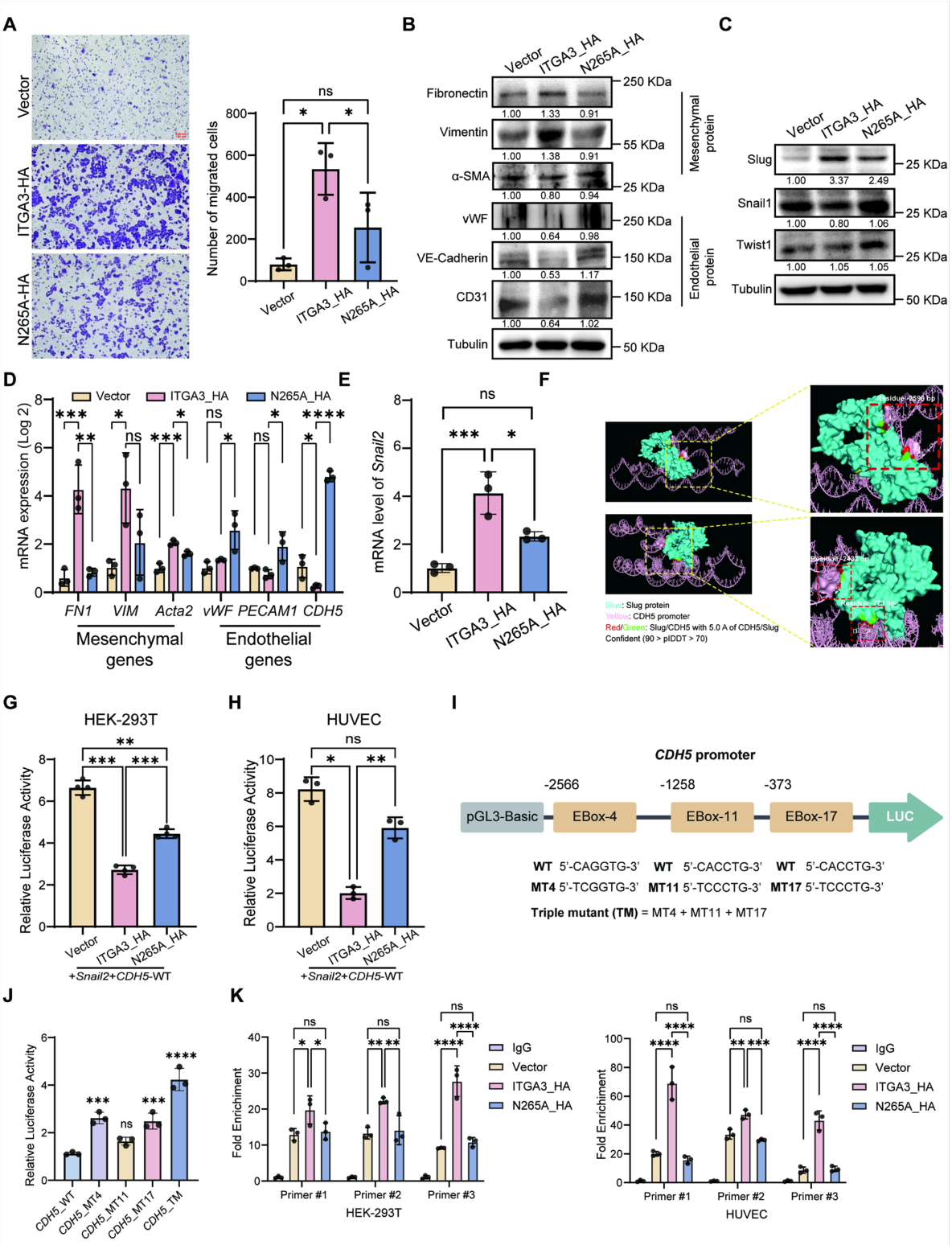


Figure 1

SLeX-modified ITGA3 promotes Slug-mediated repression of VE-cadherin and Endo-MT in ECs. A. Transwell assay of Vector, ITGA3_HA and N265A_HA cells. Scale bar: 100 μm. **B, C.** Immunoblotting for endothelial and mesenchymal markers (B), as well as Endo-MT-related transcription factors (C) in indicated ECs. **D, E.** qRT-PCR analysis for endothelial/mesenchymal markers (D) and Slug (E) expression. **F.** Predicted binding of Slug to motifs within the *CDH5* promoter using AlphaFold3. **G, H.** Dual-luciferase

reporter assays showing Slug-mediated transcriptional repression of the *CDH5* promoter in HEK-293T (G) and HUVECs (H) transfected with Vector, ITGA3_HA, or N265A_HA. **I, J.** Schematic of three predicted Slug-binding E-box motifs in the *CDH5* promoter and their mutant sequences (I), and dual-luciferase reporter assays showing loss of Slug-mediated repression and increased *CDH5* promoter activity upon individual or triple mutations (J). **K.** Quantification of Slug binding to the *CDH5*promoter by ChIP-qPCR in HEK-293T (left) and HUVECs (right) transfected with Vector, ITGA3_HA, or N265A_HA, using IgG as a negative control. Data represent means ± SEM from three independent experiments. Statistical significance was assessed by two-tailed Student's t test (*p < 0.05, **p < 0.01, ***p < 0.001, ****p < 0.0001).

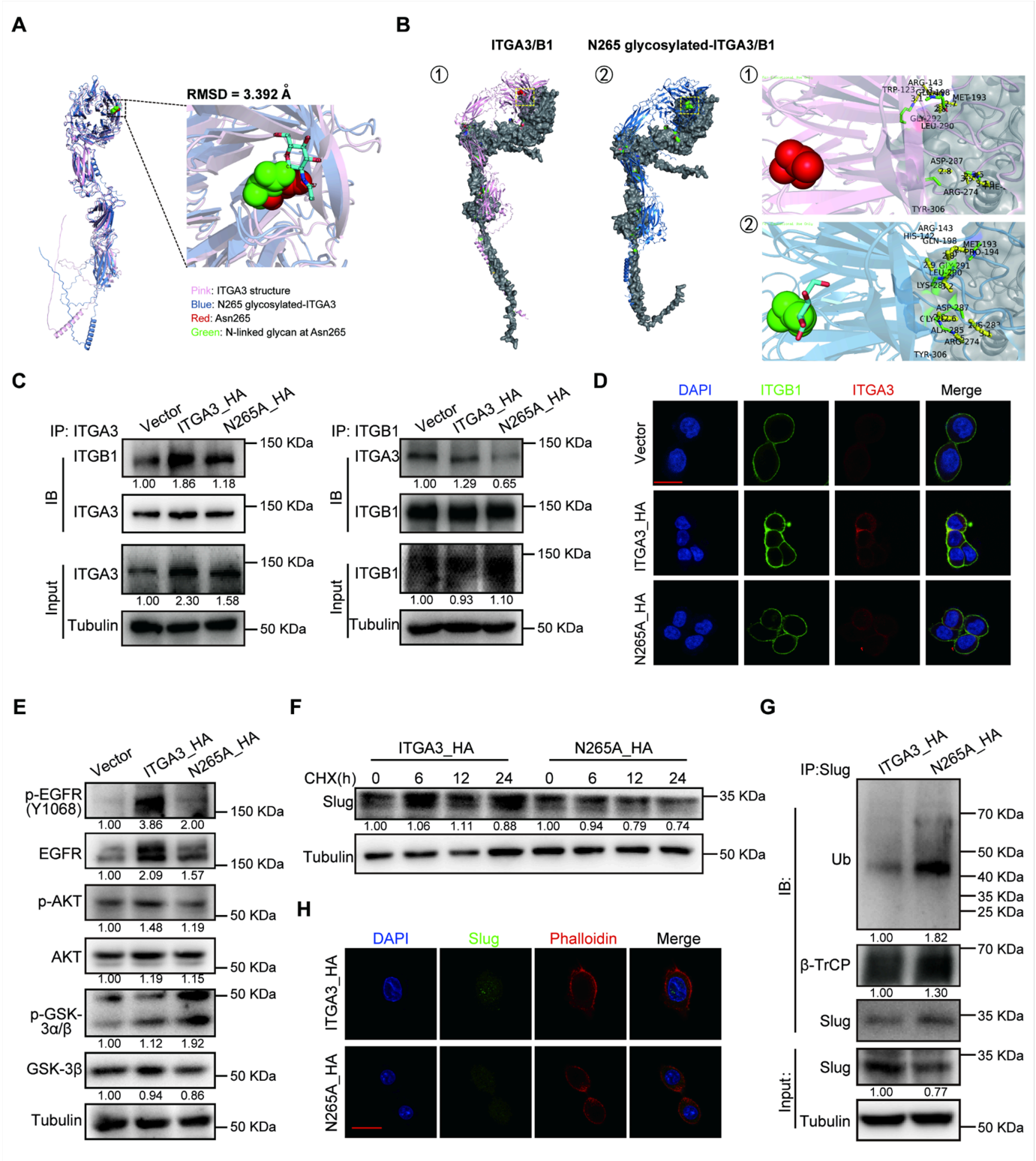


Figure 2

SLeX-modified ITGA3 stabilizes Slug through EGFR-AKT-GSK3β signaling. A. AlphaFold3-predicted structural comparison between non-glycosylated ITGA3 and N265-glycosylated ITGA3. **B.** Predicted local conformational changes at the ITGA3-ITGB1 interface induced by N265 glycosylation. **C.** Co-immunoprecipitation (Co-IP) analysis of the interaction between ITGB1 and ITGA3 in indicated ECs. **D.** Representative immunofluorescence images showing co-localization of ITGA3 and ITGB1 in ECs. Scale

bar: 20 μm. **E.** Immunoblotting of ERBB pathway components and downstream AKT-GSK3β phosphorylation in ECs with indicated transfection. **F.** Cycloheximide (CHX, 50 μg/mL) chase assay evaluating Slug protein stability in ITGA3_HA and N265A_HA cells. **G.** Co-IP analysis of Slug ubiquitination and Slug–β-TrCP interaction in ITGA3_HA and N265A_HA cells. **H.** Immunofluorescence showing Slug subcellular localization and protein levels in ECs. Scale bar: 20 μm. The data are representative of three independent experiments.

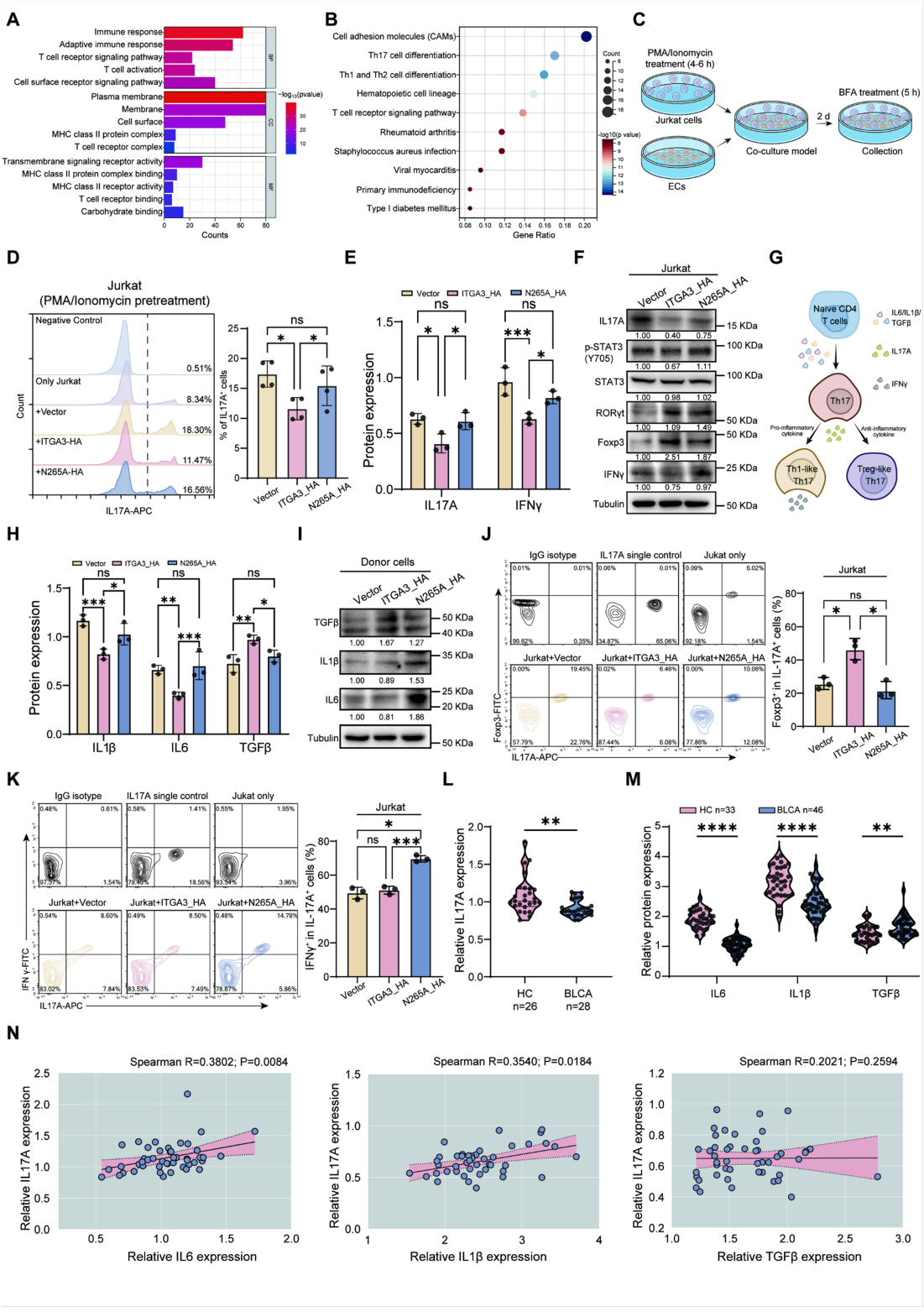


Figure 3

sLeX-modified ITGA3 in endothelial cells regulates Th17 differentiation. A, B. Gene ontology (A) and KEGG pathway analysis (B) of FUT7 co-expressed genes in BLCA patients using cBioPortal. **C.** Co-culture model of ECs (Vector, ITGA3_HA, and N265A_HA) with PMA/ionomycin pretreated Jurkat T cells. **D**. Flow cytometry analysis of $IL17A^+$ Jurkat cells following co-culture with indicated ECs. **E**. Jurkat cells stimulated by PMA and ionomycin were incubated with indicated ECs, ELISA assay for IL17A and IFNγ from Jurkat-secreted proteins. **F.** Immunoblotting of Th17, Th1 and Treg cell markers and transcription factors in Jurkat cells co-cultured with indicated ECs. **G.** Schematic of cytokine-driven Th17 differentiation and trans-differentiation. **H, I.** ELISA (H) and immunoblotting (I) assays of IL6/IL1β and TGFβ levels from medium or cell lysates of ECs. **J, K.** Flow cytometry analysis of $IFNγ^+IL17A^+$ and $Foxp3^+IL17A^+$ Jurkat cells following co-culture with ECs. **L, M.** ELISA analysis of serum IL17A (L), IL6/IL1β/TGFβ (M) levels in BLCA patients and HC. **N.** Correlation analysis of IL17A expression with IL6/IL1β/TGFβ from BLCA patients' serum. Data represent means ± SEM from three independent experiments for all cell-based assays. Statistical significance was assessed by two-tailed Student's t test, and in (N) by simple linear regression (*$p < 0.05$, **$p < 0.01$, ***$p < 0.001$, ****$p < 0.0001$).

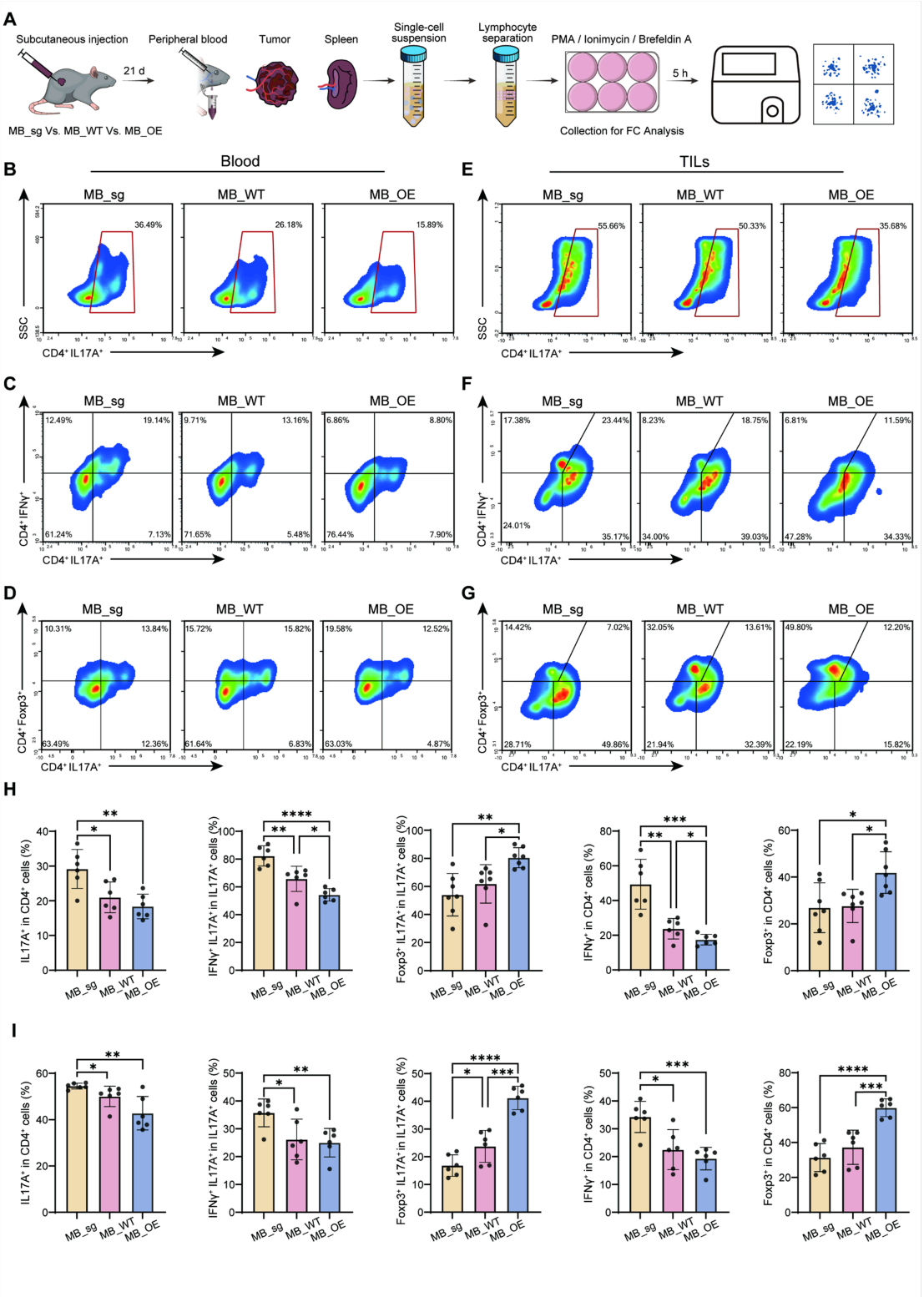


Figure 4

Enhanced sLeX glycosylation modulates CD4⁺ T cell differentiation in vivo. A. Schematic diagram of the subcutaneous tumor model and experimental workflow. **B-D.** Flow cytometry analysis of IL17A⁺ (B), IFNγ⁺IL17A⁺ (C), and Foxp3⁺IL17A⁺ (D) in $CD4^+$ T cells from peripheral blood. **E-G.** Flow cytometry of IL17A⁺ (E), IFNγ⁺IL17A⁺ (F), and Foxp3⁺IL17A⁺ (G) in $CD4^+$ T cells in TILs. **H, I.** Quantification of peripheral

blood (H) and TIL (I) results (n = 6 per group). Data represent means ± SEM. Statistical significance was assessed by two-tailed Student's t test (*p < 0.05, **p < 0.01, ***p < 0.001, ****p < 0.0001).

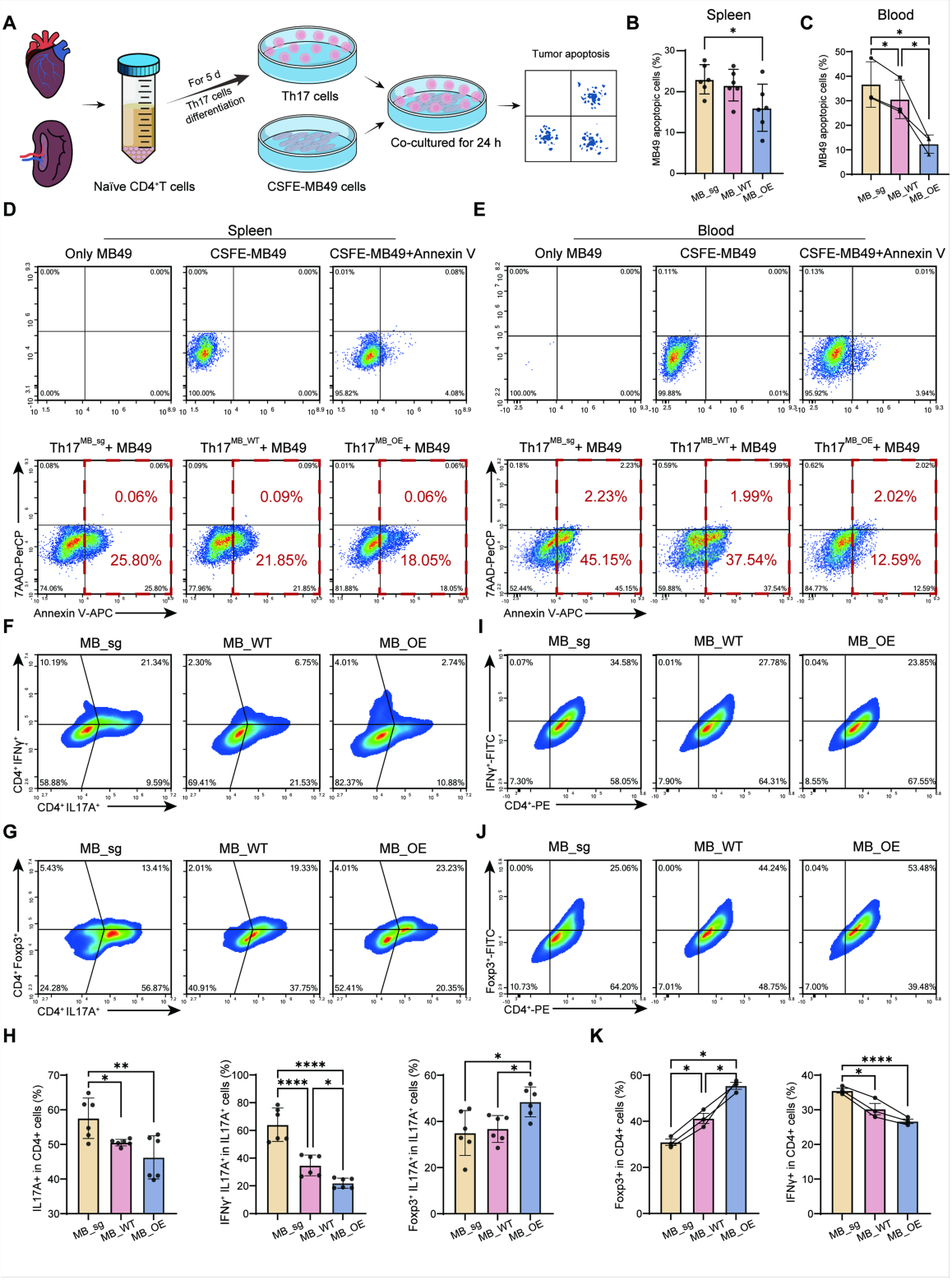


Figure 5

Enhanced sLeX glycosylation in TECs modulates Th17 cell differentiation and effector function in vivo. A. Workflow: naïve CD4⁺ T cells from spleen or peripheral blood of different mouse groups were isolated, differentiated into Th17 cells in vitro, and co-cultured with MB49 cells. **B-E.** Flow cytometry analysis of

apoptosis in MB49 co-cultured with differential Th17 cells from splenic (B, D) or peripheral blood (C, E) naïve $CD4^+$ T cells. **F-H.** Flow cytometry of $IL17A^+$, $IFN\gamma^+IL17A^+$, and $Foxp3^+IL17A^+$ in $CD4^+$ T cells after co-culturing with TECs under Th17 conditions for 5 days. **I-K.** Cells from (F, G) were switched to Th1 (I) or Treg (J) conditions for 2 additional days, flow cytometry of $IFN\gamma^+CD4^+$ and $Foxp3^+CD4^+$ cells. Sample size: n = 6/group, data are shown as 3 paired values for visualization of panels E, I and J. Data represent means ± SEM. Statistical significance was assessed by two-tailed Student's t test (*p < 0.05, **p < 0.01, ****p < 0.0001).

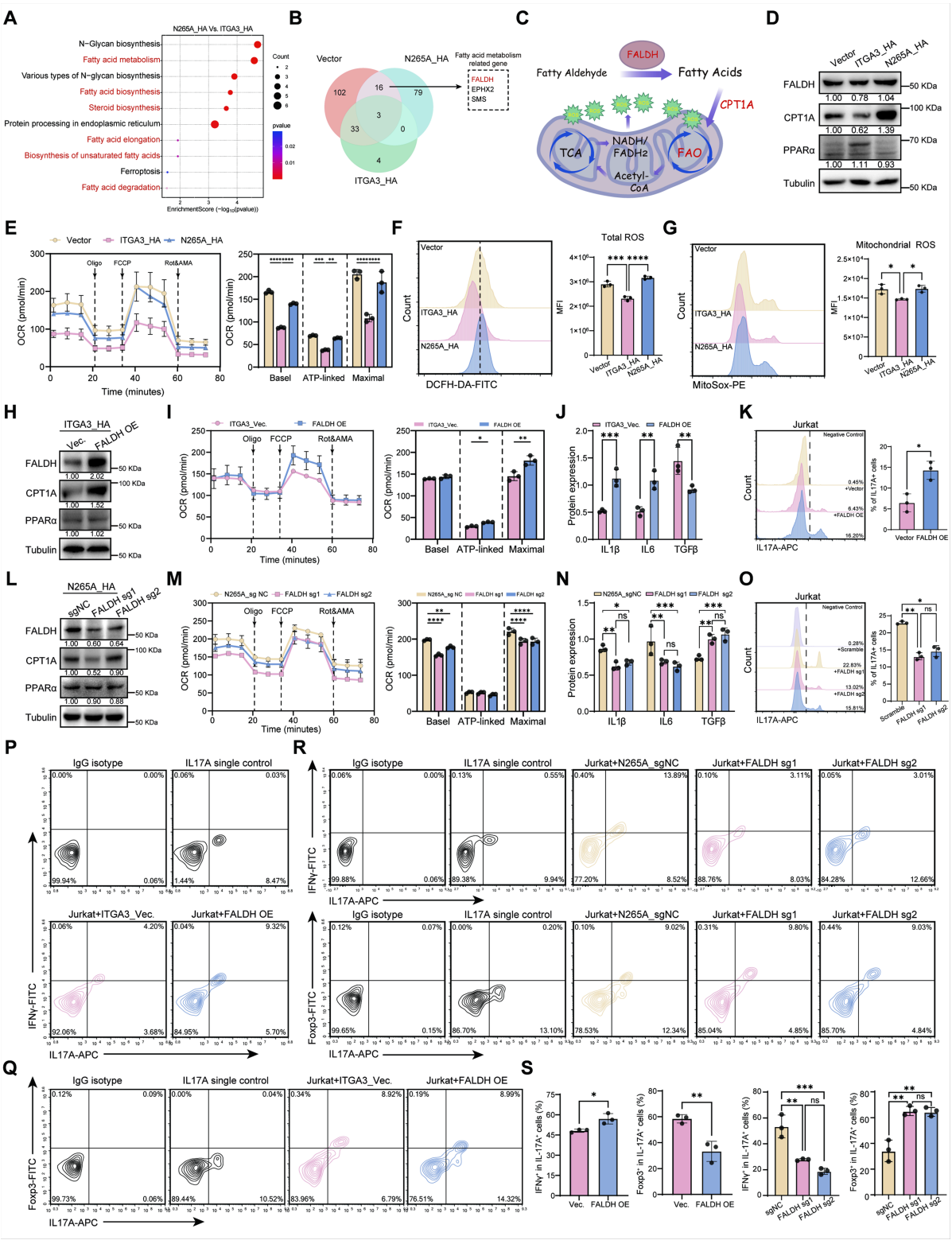


Figure 6

FALDH-mediated FAO regulates endothelial control of Th17 differentiation. A. KEGG pathway analysis of upregulated proteins in N265A_HA versus ITGA3_HA cells. **B.** Venn diagram showing commonly upregulated proteins in Vector and N265A_HA compared with ITGA3_HA. **C**. Model depicting FALDH-driven FAO and ROS generation through mitochondrial metabolism. **D.** Immunoblotting of FALDH and FAO-relate -proteins in ECs. **E.** Seahorse Cell Mito Stress Test of ECs following PA treatment. **F, G.** Flow cytometry of total and mitochondrial ROS using DCFH-DA (F) and MitoSOX (G) staining. **H.** Immunoblotting of FAO-related proteins in *FALDH*-overexpressing ITGA3_HA cells. **I.** Seahorse analysis of FAO activity in FALDH OE. **J.** ELISA of IL6/IL1β and TGFβ levels in supernatants of FALDH OE. **K.** Flow cytometry of $IL17A^+$ Jurkat cells co-cultured with FALDH OE. **L-O.** Immunoblotting of FAO-related proteins (L), Seahorse analysis of FAO activity (M), ELISA of IL6/IL1β and TGFβ in supernatants (N), and flow cytometry of $IL17A^+$ Jurkat cells co-cultured with FALDH knockout N265A_HA cells (O). **P-R.** Flow cytometry of $IFN\gamma^+IL17A^+$ and $Foxp3^+IL17A^+$ Jurkat cells co-cultured with FALDH OE (P, Q) or KO (R) ECs. **S.** Quantification of panels P-R. Data represent means ± SEM from three independent experiments. Statistical significance was assessed by two-tailed Student's t test (ns, no significance; *p < 0.05, **p < 0.01, ***p < 0.001, ****p < 0.0001).

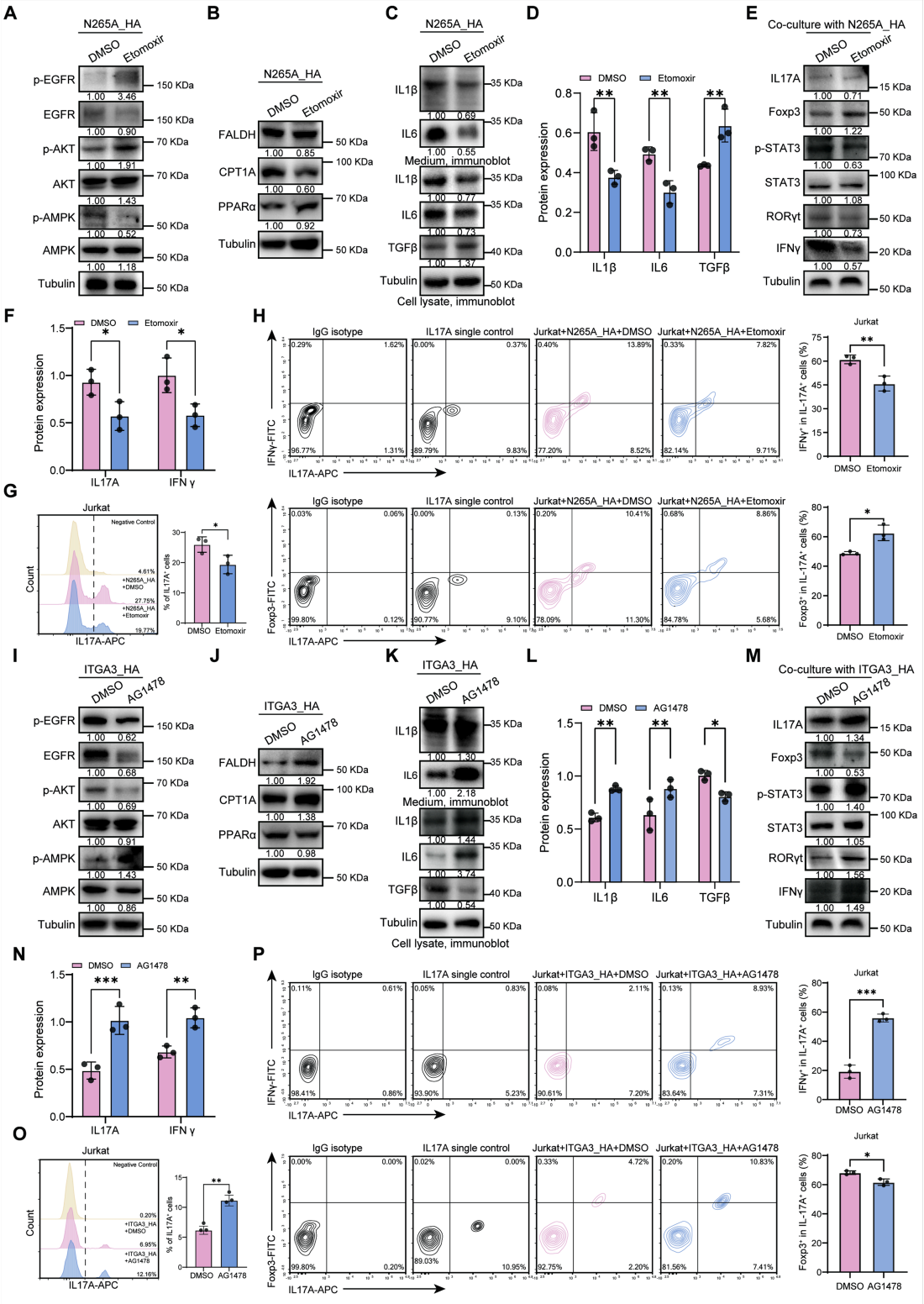


Figure 7

EGFR/AKT-AMPK signaling regulates endothelial FAO and T cell responses. A, B. Immunoblotting of EGFR/AKT-AMPK (A) and FAO related-proteins (B) in N265A_HA treated with Etomoxir. **C, D.** IL6/IL1β and TGFβ levels assessed by immunoblotting of cell lysates and supernatants (C) and by ELISA (D) of supernatants in N265A_HA after Etomoxir treatment. **E-H.** Th17-, Th1-, and Treg-associated cytokines, markers, and transcription factors analyzed by immunoblotting (E), ELISA (F), and flow cytometry (G, H)

in Jurkat cells co-cultured with Etomoxir-pretreated N265A_HA. **I-P.** Parallel analyses in ITGA3_HA cells treated with the EGFR inhibitor AG1478, including immunoblotting of EGFR/AKT–AMPK signaling and FAO-related proteins (I, J), cytokine detection by immunoblotting and ELISA (K, L), and evaluation of Th17-, Th1-, and Treg-related markers and subsets in co-cultured Jurkat cells by immunoblotting, ELISA, and flow cytometry (M-P). Data represent means ± SEM from three independent experiments. Statistical significance was assessed by two-tailed Student's t test (*p < 0.05, **p < 0.01, ***p < 0.001).

Supplementary Files

This is a list of supplementary files associated with this preprint. Click to download.

- SupplementaryTable2.xlsx
- SupplementaryTable4.xlsx
- SupplementaryTable1.xlsx
- SupplementaryTable3.xlsx
- UnprocessedWBimages.pdf
- SupplementaryMaterials.docx